Multiple Subscale Magnetic Reconnection Embedded inside a Heliospheric Current Sheet Reconnection Exhaust: Evidence for Flux Rope Merging

T. D. Phan[1] , J. F. Drake[2] , D. Larson[1] , M. Oieroset[1] , S. Eriksson[3] , Z. Yin[2] , B. Lavraud[4,5] , M. Swisdak[2] ,
S. D. Bale[1,6] , R. Livi[1] , O. Romeo[1] , P. Whittlesey[1] , J. Halekas[7] , A. Rahmati[1] , M. Pulupa[1] , A. Szabo[8] ,
A. Koval[8] , M. Moncuquet[9] , J. Kasper[10] , M. Stevens[11] , M. Desai[12] , and N. Raouafi[13]

[1] SSL, University of California, Berkeley, CA 94720, USA; phan@ssl.berkeley.edu
[2] University of Maryland, College Park, MD, USA
[3] LASP, U of Colorado, Co, USA
[4] Laboratoire d'Astrophysique de Bordeaux, Univ. Bordeaux, France
[5] IRAP, CNRS, CNES, Université de Toulouse, France
[6] Physics Department, University of California, Berkeley, CA, USA
[7] University of Iowa, Iowa City, IA, USA
[8] NASA Goddard Space Flight Center, Greenbelt, MD, USA
[9] LESIA, Observatoire de Paris-Meudon, France
[10] Climate and Space Sciences and Engineering, University of Michigan, Ann Arbor, MI, USA
[11] Smithsonian Astrophysical Observatory, Cambridge, MA, USA
[12] Southwest Research Institute, San Antonio, TX, USA
[13] Johns Hopkins University Applied Physics Laboratory, Laurel, MD, USA

Abstract

We report observations of multiple subscale reconnecting current sheets embedded inside a large-scale heliospheric current sheet (HCS) reconnection exhaust. The discovery was made possible by the unusual skimming trajectory of Parker Solar Probe through a sunward-directed HCS exhaust, sampling structures convecting with the exhaust outflows for more than 3 hr during Encounter 14, at a radial distance of ∼17 solar radii. A large number of subscale current sheets (SCSs) were detected inside the HCS exhaust. Remarkably, five SCSs showed direct evidence for reconnection, displaying near-Alfvénic outflow jets and bifurcated current sheets. The reconnecting SCSs all had small magnetic shears (27°–81°), i.e., strong guide fields. The thickness of the subscale reconnecting current sheets ranged from ∼60 km to ∼5000 km (∼20–2000 ion inertial lengths). The SCS exhausts were directed predominantly in the normal or out-of-plane direction of the HCS, i.e., nearly orthogonal to the HCS exhaust direction. The presence of multiple low-magnetic-shear reconnecting current sheets inside a large-scale exhaust could be associated with coalescence of multiple large flux ropes inside the HCS exhaust. The orientation of some SCS exhausts was partly in the ecliptic plane of the HCS, which may indicate that the coalescence process is highly three-dimensional. Since the coalescence process is likely short-lived, the detection of five such events inside a single HCS crossing could imply the common occurrence of flux rope coalescence in large-scale HCS reconnection exhausts.

Unified Astronomy Thesaurus concepts: Solar physics (1476)

1. Introduction

The heliospheric current sheet (HCS) is the largest current sheet in the solar system. It extends from the Sun to far beyond 1 au. In situ measurements of the HCS at 1 au, as well as near the Sun, have revealed that its thickness is generally thousands of ion inertial lengths or more, far exceeding the kinetic scales required for collisionless reconnection onset. Indeed, at 1 au, while reconnection exhausts have been detected in the HCS, their occurrence was deemed rare (Gosling et al. 2005b, Gosling et al. 2006; Lavraud et al. 2009). In contrast, a major surprise of the Parker Solar Probe (PSP) mission has been the common detection of reconnection exhausts in the HCS (e.g., Lavraud et al. 2020; Phan et al. 2020; Szabo et al. 2020; Phan et al. 2021), indicating that reconnection occurs almost all the time in the near-Sun HCS. Thus, the HCS near the Sun is an ideal laboratory to study the properties of large-scale reconnection.

Nearly every PSP crossing of the HCS has revealed new and often puzzling features of large-scale reconnection.

One of the interesting PSP findings is the reports of multiple magnetic flux ropes populating the HCS, based on direct imaging observations (Liewer et al. 2024), as well as the occurrence of multiple partial spacecraft crossings of the HCS exhibiting reconnection exhaust signatures (e.g., Sanchez-Diaz et al. 2019; Lavraud et al. 2020; Réville et al. 2020; Phan et al. 2021). These findings raise the questions of how these multiple flux ropes interact with each other and how they affect the dynamics of large-scale HCS reconnection. Simulations (e.g., Drake et al. 2006; Oka et al. 2010) and previous observations in the Earth's magnetosphere (e.g., Zhou et al. 2017; Wang et al. 2016) have revealed that flux ropes tend to coalesce, and the process can accelerate particles to high energies.

Here we report an Encounter 14 crossing of the HCS where a sunward-directed reconnection exhaust was detected. A large number of small-scale current sheets were present inside the large-scale HCS exhaust. We thus term these subscale current sheets (SCSs). At least five of the SCSs showed evidence for reconnection. Several of the SCSs were oriented nearly

orthogonal to the HCS, suggesting that the observed SCS reconnection could be associated with flux rope coalescence within the HCS.

2. PSP Instrumentation and Current Sheet Coordinate System

This study uses magnetic field data measured by FIELDS (Bale et al. 2016) at 290 vectors/s and proton data from SWEAP/SPAN-ion (Livi et al. 2020) and electron pitch angle information from SWEAP/SPAN-electron (Whittlesey et al. 2020), both at 0.87 s resolution.

The data will be shown in two coordinate systems. The large-scale context data in Figure 1 are shown in the RTN coordinate system, where R is the direction from the Sun to the spacecraft, T is the cross-product of the Sun's rotation vector with R, and $N = R \times T$. Individual SCSs are shown in Figures 2–4 in RTN as well as the local current sheet (XYZ) coordinate system. XYZ is determined using a hybrid minimum variance method that often works best in low-magnetic-shear current sheets (e.g., Gosling & Phan 2013; Eriksson et al. 2024; Wang et al. 2024). The SCS normal direction, Z, is determined from $B_1 \times B_2/|B_1 \times B_2|$, where B_1 and B_2 are the fields at the two current sheet edges; $Y = Z \times X'$, where X' is the maximum variance direction of the magnetic field (Sonnerup & Cahill 1967); and $X = Y \times Z$ is approximately along the direction of the reconnecting components of the magnetic field.

3. Overview of the HCS Crossing and the Presence of Sunward Exhaust

Figure 1 shows the unusually long (3.67 hr) complete crossing of the HCS on 2022 December 12 from ∼06:20 to ∼10:00 UT. The HCS is recognized by the polarity change of B_R from ∼−650 nT to ∼+470 nT (Figure 1(e)) and the switching of strahl electron pitch angle fluxes from 180° to 0° (Figure 1(c)) across the current sheet. During the first ∼50 minutes (06:20–07:10 UT), PSP crossed nearly the entire HCS based on the near-complete negative to positive B_R transition, reaching $B_R \sim 400$ nT at 07:17 UT. However, during the next ∼3 hr, PSP skimmed the $+B_R$ edge of the HCS but remained inside the HCS (see below) until it exited the HCS at ∼10:00 UT. Figure 1(h) depicts an effective PSP trajectory through the HCS. During the 3.67 hr inside the HCS, PSP traversed 1.2 R_s along the R direction, 2.4 R_s along T, and 0.1 R_s along N.

The magnetic field rotation across the HCS was ∼162°. The hybrid Alfvén speed (V_{AR}) based on B_R and the proton mass density ρ on the two sides of the HCS (Cassak & Shay 2007), $V_{AR,hybrid} = [B_{R1}B_{R2}(B_{R1}+B_{R2})/\mu_0(\rho_1 B_{R2}+\rho_2 B_{R1})]^{0.5}$, was ∼232 km s^{-1}. The available magnetic energy per particle, $m_i V_{AR}^2$, was ∼550 eV.

The hybrid minimum variance analysis yields a HCS XYZ coordinate system ($X = [0.85, -0.45, 0.19]_{RTN}$, $Y = [0.49, 0.76, -0.38]_{RTN}$, $Z = [0.02, 0.43, 0.90]_{RTN}$) that is not significantly different from RTN: the angle between R and X was ∼30° and ∼26° between N and Z.

In the frame of the ambient solar wind, there was sunward plasma jetting inside the HCS: V_R inside the HCS was ∼128 km s^{-1}, lower than the ∼235 km s^{-1} solar wind V_R flow just outside the HCS. The ΔV_R of ∼−107 km s^{-1} was ∼46% of the upstream $V_{AR,hybrid}$. The sub-Alfvénic flow speed is common for solar wind reconnection exhausts and in models of

symmetric reconnection (e.g., Liu et al. 2011; Haggerty et al. 2018). Consistent with a sunward-directed exhaust is the presence of counterstreaming 640 eV strahl electrons inside the HCS (Figure 1(c)), indicating that HCS reconnection resulted in the formation of closed magnetic field lines with both ends connected to the Sun (Gosling et al. 2006; Lavraud et al. 2009, 2020; Phan et al. 2021).

Figure 1(g) shows that the plasma density was enhanced in the HCS compared to the external solar wind, which is characteristic of symmetric reconnection. However, the density enhancement of a factor of 10 across the leading edge of the HCS was much higher than expected for reconnection exhausts (Lin & Lee 1993).

The continuous presence of a sunward reconnection jet (in solar wind frame) and the density enhancement throughout the entire 3.67 hr of HCS crossing implies that although PSP skimmed the $+B_R$ edge of the HCS, it never exited the HCS during this entire period. The skimming trajectory of PSP relative to the HCS allowed the sampling of structures convecting along the exhaust outflow direction. The 3.67 hr duration of this complete HCS crossing is much longer than previously reported complete crossings of the near-Sun HCS by PSP, which typically lasted a few minutes, up to a few tens of minutes (e.g., Phan et al. 2020, 2021; Eriksson et al. 2022, 2024).

A striking feature is the presence of many large and sharp changes of the magnetic field components inside this HCS (Figure 1(e)). Many of the changes were in B_N (red) and B_T (green), indicating the presence of SCSs embedded inside the large-scale HCS, as opposed to just multiple crossings of the HCS boundary, which would be associated with significant changes in B_R.

4. Evidence for Reconnection in SCSs

We searched for evidence for reconnection within all individual SCSs. Table 1 lists the five unambiguous reconnection events that we have been able to identify, as well as their properties in terms of exhaust width and orientation, magnetic shear, and plasma jet speed compared to the upstream Alfvén speed. Reconnection jets are bounded on one edge of the current sheet by correlated changes in velocity, V, and magnetic field, B, and anticorrelated changes in V and B on the other edge, consistent with Alfvénic disturbances propagating in opposite directions along reconnected field lines away from the X-line (Gosling et al. 2005a).

For each event, we will show the data in RTN as well as XYZ coordinates. Reconnection jet signatures are clearest in XYZ, while the jet velocity in RTN gives indication of how the reconnection exhaust outflow (X) direction is oriented relative to the HCS. We will be presenting events 2–5 before event 1, as they have standard reconnection signatures. Event 1 is more complex as it appears to have an additional secondary reconnection occurring at one edge of an SCS reconnection exhaust.

4.1. Subscale Reconnection Events 2–5

Event 2. Figures 2(a)–(d) show a 12 s interval around a SCS with a sharp positive change in B_N labeled "2" in Figure 1(e). The current sheet was bifurcated, with sharp changes in the reconnecting component of the magnetic field, B_X, at the two
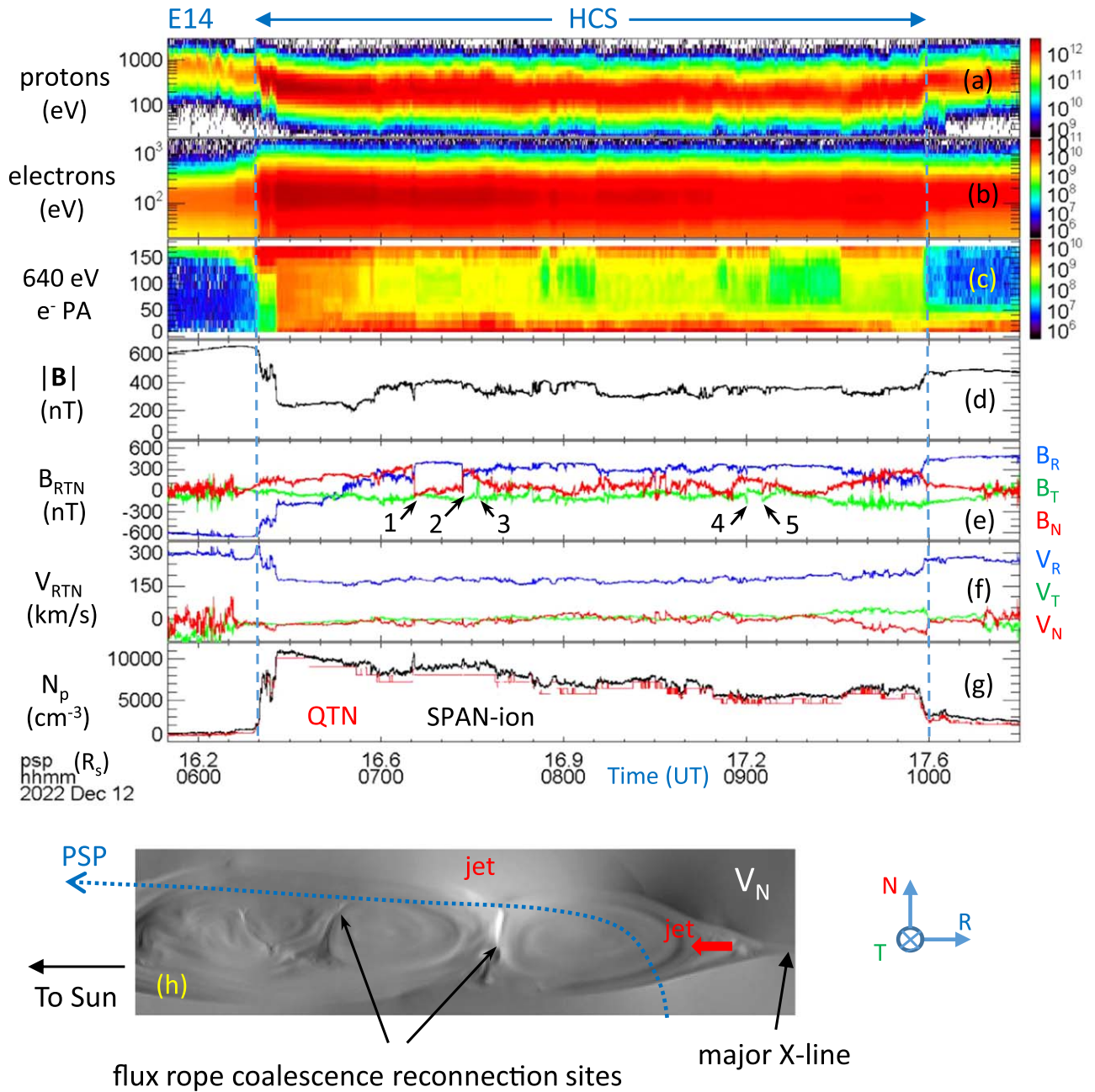
Figure 1. Long-duration (3.67 hr) PSP crossing of a sunward-directed HCS reconnection exhaust during E14. (a), (b) Proton and electron spectrograms in differential energy flux (eVs^{-1} cm^{-2} ster^{-1} eV^{-1}); (c) pitch angle distribution of 640 eV electrons; (d), (e) magnetic field magnitude and components in RTN coordinates; (f) proton velocity in RTN; (g) density measured by SWEAP/SPAN-ion instrument (back) and from FIELDS/Quasi-Thermal Noise spectroscopy (red). The multi-island coalescence shown in panel (h) is from a kglobal simulation of reconnection (Yin et al. 2024) and serves as a sketch to illustrate the effective trajectory of PSP quickly crossing much of the HCS, followed by skimming near one edge of the HCS for a long time. The vertical blue dashed lines in panels (a)–(g) mark the edges of the HCS. The proton velocity is in the Sun's frame, while the spectrograms are in the spacecraft frame. PSP remained inside the HCS during the entire 3.67 hr. Five SCSs exhibiting reconnection jets are labeled in panel (e).

edges of the current sheet and a plateau in the middle (Figure 2(c)). The exhaust was identified by the presence of a positive V_X jet (Figure 2(d)) in the region where the magnetic field rotated (Figures 2(a), (c)), with changes in V_x and B_x being correlated on the leading edge and anticorrelated on the trailing edge. The peak V_X jet speed was ~23 km s^{-1} relative to the average V_X on the two sides of the SCS or 67% of the hybrid Alfvén speed of 34 km s^{-1} based on B_X and the proton mass density ρ on the two sides of the SCS. The magnetic shear across the current sheet was low, $\theta_B \sim 48°$, i.e., the guide field was ~2.2 times the reconnecting field. The SCS thickness was

~217 km (or 95 ion inertial lengths, d_i) based on an SCS crossing duration of 2.9 s and an SCS normal (Z) velocity (relative to the spacecraft) of 76 km s^{-1}.

Importantly, the SCS was oriented nearly orthogonal to the HCS, with the antiparallel field direction, $X = [-0.45, -0.04, 0.89]_{RTN}$, being predominantly in the N direction. This is consistent with B_N showing the largest transition across the SCS (Figure 2(a)) and the largest exhaust jet being in N (Figure 2(b)). Interestingly, the SCS normal direction, $Z = [0.2, 0.95, 0.23]_{RTN}$, was mostly along T, nearly orthogonal to the HCS normal direction.
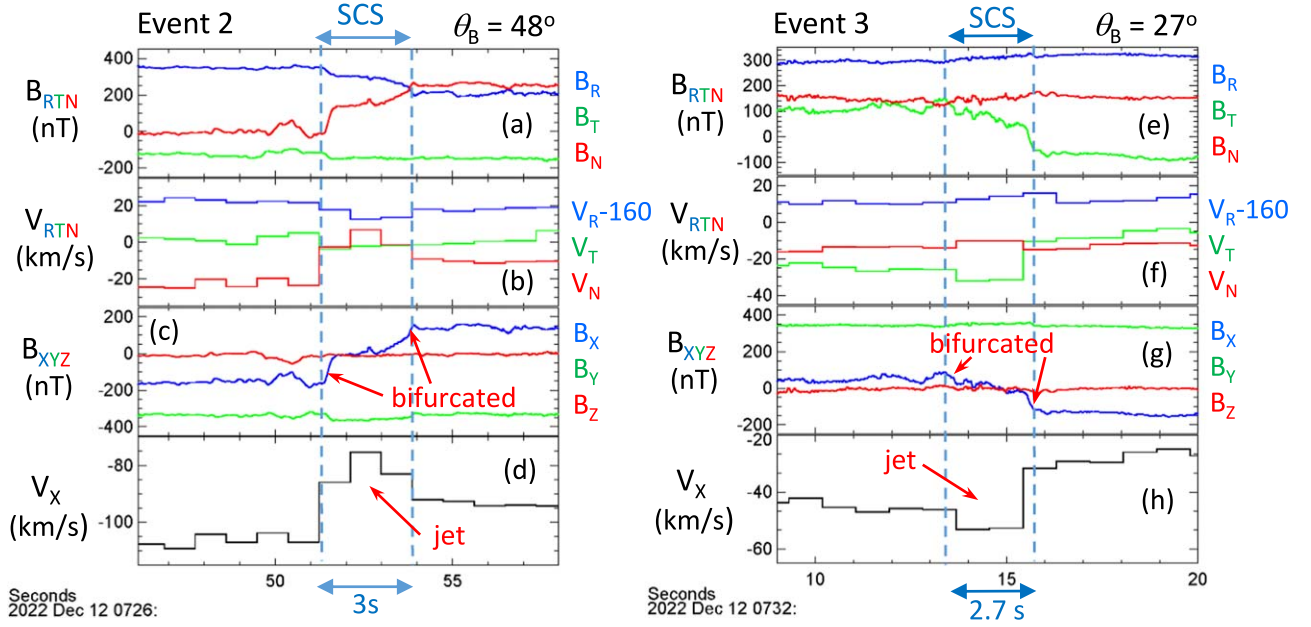
Figure 2. Examples "2" and "3" of reconnection in SCSs embedded inside the HCS exhaust. Their locations are marked in Figure 1(e). (a), (e) Magnetic field in RTN; (b), (f) proton velocity in RTN; (c), (g) magnetic field in the XYZ SCS coordinate system; (d), (h) X component of the velocity. The parameters are the same as in Figure 2. The vertical blue dashed lines mark the two edges of the SCS based on magnetic field data, which have higher temporal resolution than proton data. The XYZ coordinate system is shown in Figure 4(i).

Event 3. The next example, labeled "3" in Figure 1(e), also shows a bifurcated current sheet (Figure 2(g)) with an embedded negative V_X plasma jetting (Figure 2(h)). The peak V_X jet speed relative to the average V_X on the two sides of the SCS was $\sim 15.9 \, \text{km s}^{-1}$ or 96% of the upstream hybrid Alfvén speed of this SCS of $\sim 16.6 \, \text{km s}^{-1}$. ΔV_X was smaller across the leading edge compared to the trailing edge due to the presence of a V_X velocity shear across the current sheet (Eriksson et al. 2009). The ΔB_X transition was also smaller at the leading edge, such that the velocity change was roughly Alfvénic across each edge of the SCS. The magnetic shear associated with this SCS was only $\sim 27°$ (guide field ~ 4). The exhaust was directed predominantly in the **T** direction ($X = [0.16, \ 0.98, \ -0.08]_{\text{RTN}}$), consistent with the main magnetic field rotation being in B_T (Figure 2(e)) and the dominant jet component being V_T (Figure 2(f)). The current sheet width was $\sim 176 \, \text{km}$ ($72 \, d_i$).

Event 4. The next event, labeled "4" in Figure 1(e), is the thinnest of the five reconnecting SCSs and is at the limit of proton measurement cadence. The crossing duration of the SCS was only 0.75 s (Figure 3(a)), slightly less than a 0.87 s SPAN-ion sampling time. Nevertheless, there was a clear outflow V_X jet of $\sim 15 \, \text{km s}^{-1}$ (Figure 3(d)) or $\sim 60\%$ of the hybrid Alfvén speed for this SCS of $25 \, \text{km s}^{-1}$. The true jet speed is likely higher if the SCS could be better resolved. The thin current sheet was bifurcated, and the magnetic shear, θ_B, was $\sim 30°$ (guide field ~ 3.7). The current sheet width was $\sim 62 \, \text{km}$ ($20 \, d_i$). The durations of the sharp (B_X) exhaust boundary crossings on both sides were $\sim 0.2 \, \text{s}$, which translate to $\sim 17 \, \text{km}$ ($5 \, d_i$).

The exhaust was directed predominantly in the **T** direction, $X = [0.43, 0.90, -0.02]_{\text{RTN}}$, consistent with the fact that the V_T jet (Figure 3(b)) and the associated B_T transition (Figure 3(a)) were the largest component compared to the R and N components.

Event 5. Event "5" in Figure 1(e) is again characterized by a bifurcated current sheet with an embedded jet. The crossing

duration of the current sheet was only 1.6 s (Figure 3(e)). Nevertheless, the jet is clearly seen in V_X (Figure 3(h)), as well as in the RTN components of the velocity (Figure 3(f)). It is difficult to determine precisely the external V_X in this case because the velocity samples immediately preceding and following the SCS may contain part of the SCS itself, making it difficult to determine ΔV_X across the current sheet edges. However, the ΔV_X was at least $15 \, \text{km s}^{-1}$, compared to the hybrid Alfvén speed of $34 \, \text{km s}^{-1}$. The magnetic shear, θ_B, of this event was $43°$ (guide field ~ 2.5). The SCS thickness was $62 \, \text{km}$ ($20 \, d_i$). The durations of the sharp (B_X) exhaust boundary crossings were $\sim 0.3 \, \text{s}$, which correspond to $\sim 12 \, \text{km}$ ($4 \, d_i$). With $X = [0.11, 0.57, 0.81]_{\text{RTN}}$, the exhaust was directed predominantly along **N**, nearly orthogonal to the HCS exhaust direction.

4.2. Subscale Reconnection Events 1

Figures 4(a)–(d) shows the event labeled "1" in Figure 1(e), where a sharp negative B_N transition was observed together with a significant change in the B_R component. At first glance, the event appeared to be a classic reconnecting current sheet with a (positive) V_X jet (Figure 4(d)) spanning a bifurcated current sheet with two sharp B_X transitions at the two current sheet edges and a plateau in B_X in the middle (Figure 4(c)). However, on closer inspection, at the trailing edge of the current sheet ($\sim 07{:}11{:}05 \, \text{UT}$), there was an additional current sheet bifurcation, with two steps in B_x and a plateau in the middle. Thus, this current sheet is trifurcated rather than the usual bifurcation for reconnection exhausts. Figures 4(e)–(h) show a 20 s zoom in of the trailing edge B_X transition at around $07{:}11{:}05 \, \text{UT}$. This "edge current sheet" (termed event 1b) appears to be a stand-alone reconnecting current sheet, with current sheet bifurcation and an embedded V_X jet (Figures 4(g), (h)). However, the V_X jet was directed in the negative X direction, opposite to the positive V_X jet in the larger current sheet to the left of it.
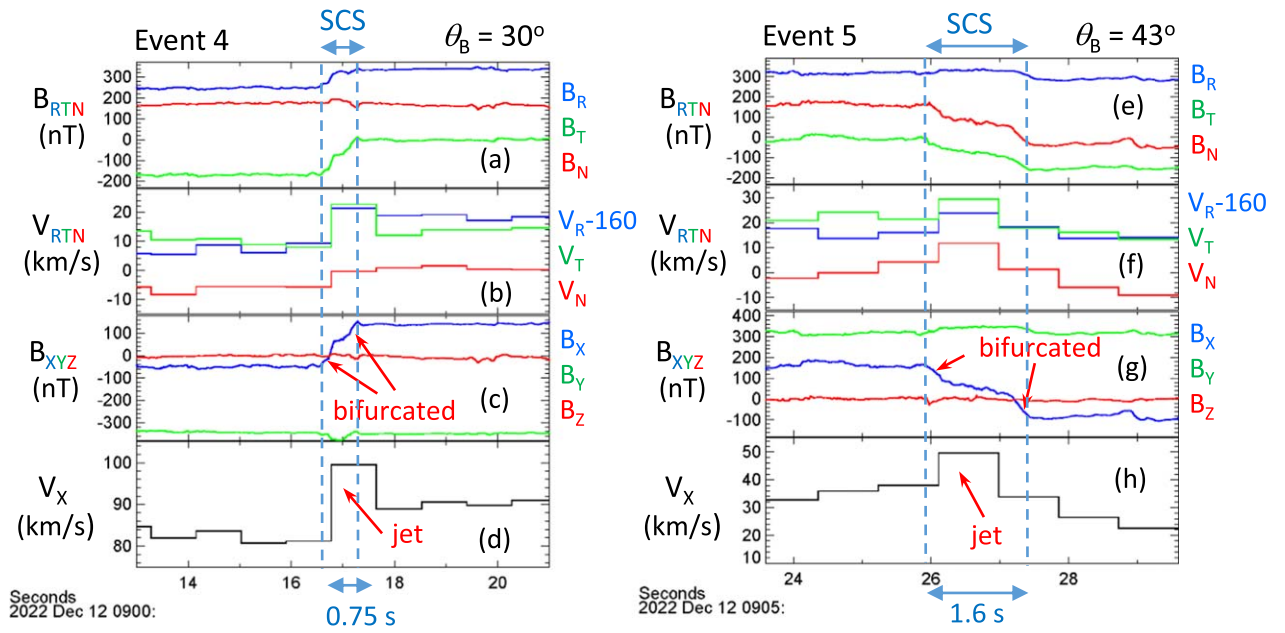
Figure 3. Examples "4" and "5" of reconnection in the SCSs embedded inside the HCS exhaust. The parameters are the same as in Figure 2.

Although rare, trifurcated current sheets, with opposite jets adjacent to each other, have been reported before (Eriksson et al. 2022, 2024) in some solar wind current sheets not associated with the HCS. Eriksson et al. (2022) interpreted this phenomenon as secondary reconnection occurring at the current sheet associated with the sharp boundary of the primary reconnecting current sheet. A possible scenario is depicted in Figure 4(i). In this scenario, the primary exhaust is bounded by the two blue vertical dashed lines in Figures 4(a)–(d) (termed event 1a) and is shaded light blue in Figure 4(i). Event 1b (Figures 4(e)–(h)) results from reconnection at the current sheet at the trailing edge of the primary exhaust. The resulting secondary reconnection exhaust is shaded yellow in Figure 1(i). The magnetic shears of SCS 1a and 1b were 81° and 61°, respectively. The peak V_X jet speed (relative to the average Vx outside the current sheet) was 52% and 76% of the hybrid Alfvén speed for SCS 1a and 1b, respectively. Note that inside the SCS 1a exhaust, V_X decreased after reaching its peak near 07:10:28 UT, such that there was essentially no flow change across the right edge of SCS 1a (if one ignores the secondary jet associated with SCS 1b). This flow slowdown is further evidence of the complexity of this event—the slowdown is likely due to the presence of a secondary flux rope downstream (sunward) from the spacecraft.

For both SCS 1a ($X = [−0.48, −0.08, 0.87]_{RTN}$) and 1b ($X = [−0.49, −0.07, 0.87]_{RTN}$), their exhausts were directed predominantly in the N direction at large angles to the HCS exhaust. The current sheet normals (Z direction) of both SCSs were mostly in the T direction (see Table 1).

5. Summary and Discussions

We have described observations of magnetic reconnection in SCSs embedded inside a large-scale HCS reconnection exhaust. The discovery was made possible by the unusual skimming trajectory of PSP through a HCS, sampling the sunward-directed HCS reconnection exhaust for 3.67 hr and crossing a large number of SCSs within the HCS exhaust. Five of the SCSs displayed plasma jetting consistent with

reconnection. Remarkably, although we did not identify reconnection exhausts based on magnetic field profiles, all five SCS exhausts identified based on the presence of plasma jetting showed current sheet bifurcation similar to bifurcation seen in many large-scale solar wind reconnecting current sheets, including the HCS (e.g., Gosling et al. 2005a; Phan et al. 2006; Gosling & Szabo 2008; Mistry et al. 2015; Phan et al. 2020), suggesting that the HCS and SCS are self-similar, both being bounded by shock-like structures. Measurements in the solar wind revealed current sheets at various scales, also suggesting self-similarity (Greco et al. 2016). The thickness of the sharp SCS exhaust boundaries was a few ion inertial lengths, i.e., at kinetic scales. Theoretically, the formation of bifurcated current sheets remains poorly understood. While Petschek (1964) slow shocks with bifurcated current sheets have been produced in MHD simulations (Sato & Hayashi 1979), they are not typically seen in fully kinetic simulations (Liu et al. 2011).

The width of the SCS ranged from 62 km to 4800 km (20–2000 ion inertial lengths). The duration of the SCS crossing was less than 3 s in three of the events, i.e., near the limit of the plasma measurement cadence. There are likely additional reconnection events in some observed superthin bifurcated SCSs that could not be resolved by the plasma measurements.

A key question is what SCS reconnection embedded in a large-scale exhaust represents. Reconnection exhausts are often turbulent (e.g., Eastwood et al. 2009; Pucci et al. 2017; Ergun et al. 2018), containing filamentary thin current sheets (e.g., Daughton & Karimabadi 2007; Phan et al. 2016). Such turbulent current sheets could undergo intermittent reconnection (e.g., Matthaeus & Lamkin 1986; Retinò et al. 2007; Servidio et al. 2009; Osman et al. 2014; Phan et al. 2018; Stawarz et al. 2019; Califano et al. 2020; Franci et al. 2022). The orientations of current sheets in a fully turbulent exhaust should have random directions (Donato et al. 2012).

In contrast, the orientations of the SCS reported here were nearly perpendicular to the HCS. Furthermore, the observed SCS were bifurcated, suggesting that the SCS exhausts were
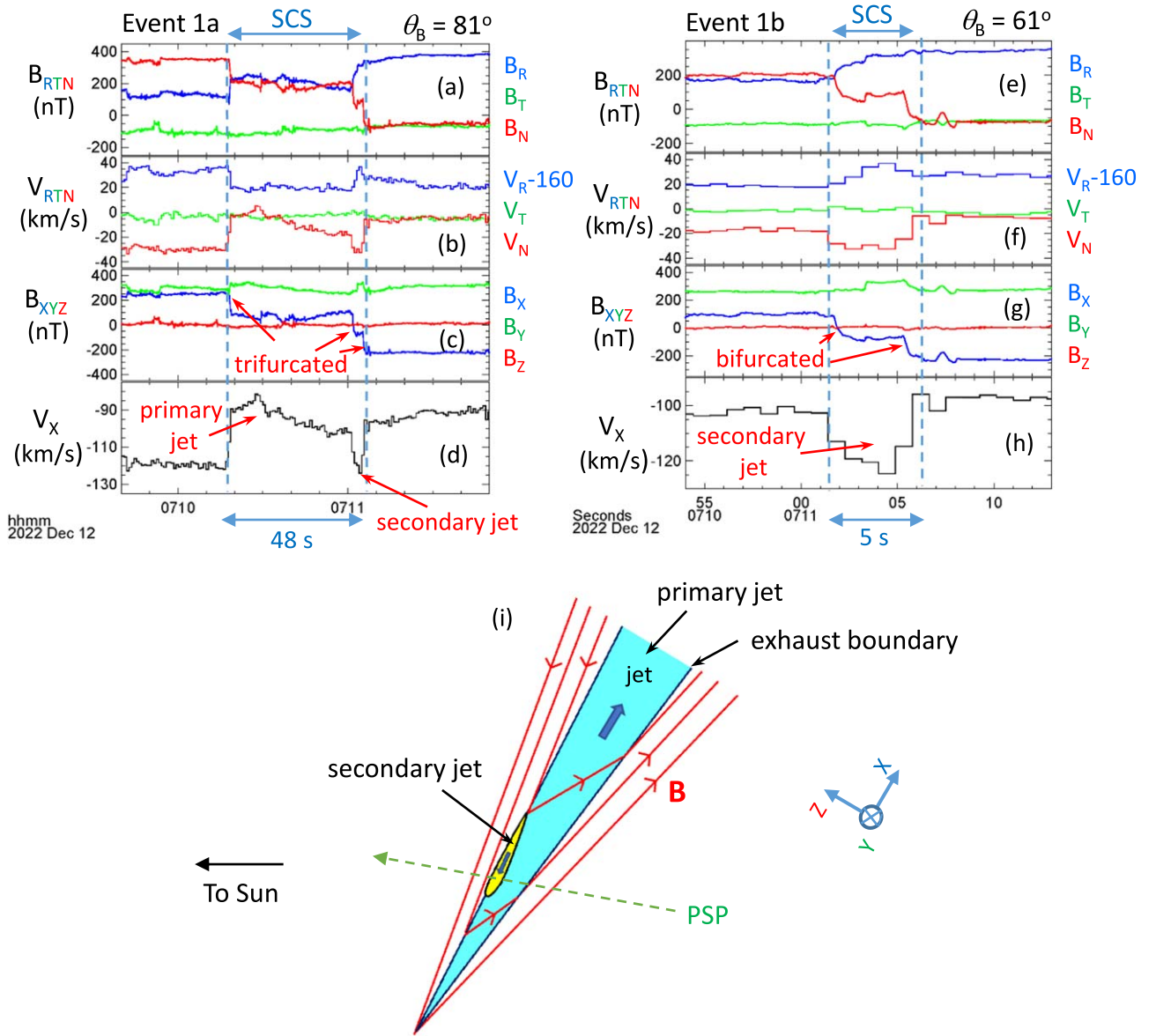
Figure 4. Example "1" of reconnection in the SCSs embedded inside the HCS exhaust. SCS "1b" is located at the trailing edge of SCS "1a." Parameters a–h are the same as in Figure 2. (i) Schematic of the PSP crossing of possible secondary reconnection exhaust (shaded yellow) occurring at the trailing edge of the primary SCS reconnection exhaust.

fully developed. These features are more consistent with predictions from flux rope coalescence (Drake et al. 2006; Oka et al. 2010; Huang & Bhattacharjee 2010; Fermo et al. 2011; Khabarova et al. 2015; Khabarova & Zank 2017; Arnold et al. 2021). In the coalescence/merging scenario, the PSP detections of a large number of B_N reversals in the HCS (Figure 1(e)) of various amplitudes and sharpness could be consistent with the presence of magnetic flux ropes of various scale sizes inside the HCS (Crooker et al. 1996; Viall et al. 2010; Liewer et al. 2024). The occurrence of reconnection at some of the sharp magnetic field changes could be indicative of reconnection at the interface of magnetic flux ropes during the coalescence process. The fact that the outflow direction of the SCS exhaust often points nearly perpendicular to the HCS outflow direction would be consistent with the coalescence scenario.

One of the intriguing features of the reconnecting SCSs is that all five identified events had low magnetic shear ($<81°$) in contrast to the high magnetic shear ($162°$) across the large HCS

itself. A possible explanation is that the out-of-plane fields in the HCS were enhanced due to compression in magnetic flux ropes. This was evident in computer simulations of this event (M. Desai et al. 2024, in preparation). Reconnection involving these regions of enhanced guide field would have lower magnetic shear. Furthermore, as the coalescence process progresses, the magnetic shear between the merging flux ropes should gradually decrease as the reconnection reaches the core of flux ropes, where the reconnecting component of the magnetic field is smaller than the out-of-plane component. This scenario could also be consistent with some observed SCS exhausts directed predominantly in the T direction (approximately the HCS out-of-plane direction), indicating that the coalescence process is highly three-dimensional. The much larger than expected density compression (>4) in the HCS (described in Section 3) could also be due to compression associated with magnetic flux ropes and flux rope merging in this HCS (e.g., Drake et al. 2006; Li et al. 2018; Øieroset et al. 2023).

Table 1
List of Reconnection Events in SCSs inside HCS on 2022 December 12

Event	Start–End times[a] (UT)	Crossing dur[b] (s)	$\lvert V_Z \rvert$[c] (km s^{-1})	Width[d] (km)	Width[e] (d_i)	B_{Guide}[f]	θ[g] (deg)	SCS XYZ Coordinates in RTN[h]	$V_{\text{AX, hybrid}}$[i] (km s^{-1})	$\lvert \Delta V_X \rvert$[j] (km s^{-1})
1a	07:10:18.000–07:11:04.579	48.0	101	4860	2020	1.2	81	[−0.48, −0.08,0.87] [0.84, −0.31,0.44] [0.23,0.95,0.22]	56.0	29.0
1b	07:11:01.210–07:11:06.900	5.7	99	563	249	1.7	61	[−0.49, −0.07,0.87] [0.83, −0.32,0.45] [0.24,0.94,0.22]	32.9	24.9
2	07:26:51.009–07:26:53.869	2.9	76	217	95	2.2	48	[−0.45, −0.04,0.89] [−0.81,0.44, −0.39] [−0.37, −0.90, −0.23]	33.8	22.8
3	07:32:13.319–07:32:16.049	1.1	65	176	72	4.1	27	[−0.16,0.98, −0.08] [0.89,0.18,0.42] [0.43,0.00, −0.90]	16.6	15.9
4	09:00:16.536–09:00:17.289	0.75	83	62	20	3.7	30	[0.43,0.90, −0.02] [−0.78,0.36, −0.50] [−0.45,0.23,0.86]	24.9	14.8
5	09:05:25.900–09:05:27.450	1.55	40	62	20	2.5	43	[0.11,0.57,0.81] [0.94, −0.32,0.10] [0.31,0.76,0.57]	34.0	>15

Notes.
[a] Crossing times of leading and trailing edges of the SCS.
[b] Duration of the SCS crossing.
[c] Average normal (Z) velocity measured at the two edges of the SCS, representing SCS normal motion relative to PSP.
[d] Width of the SCS, obtained from the crossing duration and normal velocity.
[e] Width of the SCS in the ion inertial length based on the average density measured at the two edges of the SCS.
[f] Guide magnetic field $= \tan(90° \text{-}\theta_B/2)$, a measure of the out-of-plane magnetic field relative to the reconnecting field.
[g] Magnetic shear angle θ_B across the SCS.
[h] SCS (XYZ) coordinate system obtained from hybrid minimum variance analysis of the magnetic field.
[i] X component of the hybrid Alfvén velocity based on B_X and mass density on the two sides of the SCS.
[j] Peak V_X speed in the SCS relative to the average V_X on the two sides of the SCS.

Since the coalescence process is believed to be short-lived, the detection of five such events inside a single HCS crossing would suggest the common occurrence of flux rope coalescence in large-scale HCS reconnection exhausts.

Simulations have suggested that magnetic island coalescence leads to efficient production of suprathermal particles (e.g., Drake et al. 2010, 2013; Oka et al. 2010; Arnold et al. 2021). Thus, our finding could have important implications for the understanding of energetic particle production in large-scale reconnection exhausts. Indeed, nonthermal proton acceleration up to ∼40 keV was observed in an Encounter 8 HCS exhaust (Phan et al. 2022) and up to 500 keV in the present (Encounter 14) HCS (M. Desai 2024, in preparation), both far exceeding the ∼200–500 eV available magnetic energy per particle in the ambient solar wind for these events.

Acknowledgments

ORCID iDs

T. D. Phan https://orcid.org/0000-0002-6924-9408
J. F. Drake https://orcid.org/0000-0002-9150-1841
D. Larson https://orcid.org/0000-0001-5030-6030
M. Oieroset https://orcid.org/0000-0003-3112-1561
S. Eriksson https://orcid.org/0000-0002-5619-1577
Z. Yin https://orcid.org/0009-0009-7643-6103
B. Lavraud https://orcid.org/0000-0001-6807-8494
M. Swisdak https://orcid.org/0000-0001-9898-464X
S. D. Bale https://orcid.org/0000-0002-1989-3596
R. Livi https://orcid.org/0000-0002-0396-0547
O. Romeo https://orcid.org/0000-0002-4559-2199
P. Whittlesey https://orcid.org/0000-0002-7287-5098
J. Halekas https://orcid.org/0000-0001-5258-6128
A. Rahmati https://orcid.org/0000-0003-0519-6498
M. Pulupa https://orcid.org/0000-0002-1573-7457
A. Szabo https://orcid.org/0000-0003-3255-9071
A. Koval https://orcid.org/0000-0003-1398-1752
M. Moncuquet https://orcid.org/0000-0002-9621-0365
J. Kasper https://orcid.org/0000-0002-7077-930X
M. Stevens https://orcid.org/0000-0002-7728-0085
M. Desai https://orcid.org/0000-0002-7318-6008
N. Raouafi https://orcid.org/0000-0003-2409-3742

References

Arnold, H., Drake, J. D., Swisdak, M., et al. 2021, PhRvL, 126, 13
Bale, S. D., Goetz, K., Harvey, P. R., et al. 2016, SSRv, 204, 49
Cassak, P. A., & Shay, M. A. 2007, PhPl, 14, 102114
Califano, F., Cerri, S., Faganello, M., et al. 2020, FrP, 8, 317
Crooker, N. U., Burton, M. E., Siscoe, G. L., et al. 1996, JGRA, 101, 24331
Daughton, William, & Karimabadi, Homa 2007, PhPl, 14, 072303
Donato, S., Servidio, S., Dmitruk, P., et al. 2012, PhPl, 19, 092307
Drake, J. F., Swisdak, M., Schoeffler, K. M., Rogers, B. N., & Kobayashi, S. 2006, GeoRL, 33, L13105
Drake, J. F., Opher, M., Swisdak, M., & Chamoun, J. N. 2010, ApJ, 709, 963
Drake, J. F., Swisdak, M., & Fermo, R. 2013, ApJ, 763, L5
Eastwood, J. P., Phan, T. D., Bale, S. D., & Tjulin, A. 2009, PhRvL, 102, 035001
Ergun, R. E., Goodrich, K. A., Wilder, F. D., et al. 2018, GeoRL, 45, 3338
Eriksson, S., Gosling, J. T., Phan, T. D., et al. 2009, JGRA, 114, A07103
Eriksson, S., Swisdak, M., Mallet, A., et al. 2024, ApJ, 965, 76
Eriksson, S., Swisdak, M., Weygand, J., et al. 2022, ApJ, 933, 181
Fermo, R. L., Drake, J. F., Swisdak, M., & Hwang, K.-J. 2011, JGRA, 116, A9
Franci, L., Papini, E., Micera, A., et al. 2022, ApJ, 936, 27
Gosling, J. T., Skoug, R. M., McComas, D. J., & Smith, C. W. 2005a, JGRA, 110, A01107
Gosling, J. T., Skoug, R. M., McComas, D. J., & Smith, C. W. 2005b, GeoRL, 32, L05105
Gosling, J. T., McComas, D. J., Skoug, R. M., & Smith, C. W. 2006, GeoRL, 33, L17102
Gosling, J. T., & Szabo, A. 2008, JGRA, 113, A10103
Gosling, J. T., & Phan, T. D. 2013, ApJL, 763, L39
Greco, A., Perri, S., Servidio, S., et al. 2016, ApJ, 823, L39
Haggerty, C. C., Shay, M. A., Chasapis, A., et al. 2018, PhPl, 25, 102120
Huang, Y. M., & Bhattacharjee, A. 2010, PhPl, 17, 062104
Khabarova, O., Zank, G., Li, G., et al. 2015, ApJ, 808, 181
Khabarova, O. V., & Zank, G. P. 2017, ApJ, 843, 4
Lavraud, B., Fargette, N., Reville, N., et al. 2020, ApJS, 894, L19
Lavraud, B., Gosling, J. T., Rouillard, A. P., et al. 2009, SoPh, 256, 379
Li, X., Guo, F., Li, H., et al. 2018, ApJ, 855, 80
Liewer, P. C., Gallagher, B. M., Stenborg, G., et al. 2024, ApJ, 970, 79
Lin, Y., & Lee, L. C. 1993, SSRv, 65, 59
Liu, Y. H., Drake, J. F., & Swisdak, M. 2011, PhPl, 18, 092102
Livi, R., Larson, D. E., Kasper, J. C., et al. 2020, esoar, 105, essoar.10508651
Matthaeus, W. H., & Lamkin, S. L. 1986, PhFl, 29, 2513
Mistry, R., Eastwood, J. P., Phan, T. D., & Hietala, H. 2015, GeoRL, 42, 10513
Oka, M., Phan, T. D., Krucker, S., et al. 2010, ApJ, 714, 915
Øieroset, M., Phan, T. D., Oka, M., et al. 2023, ApJ, 954, 118
Osman, K. T., Matthaeus, W. H., Gosling, J. T., et al. 2014, PhRvL, 112, 215002
Petschek, H. E. 1964, in Proc. of the AAS-NASA Symp., ed. N. H. Wilmot (Washington, DC: NASA, Science and Technical Information Division), 425
Phan, T. D., Bale, S. D., Eastwood, J. P., et al. 2020, ApJS, 246, 34
Phan, T. D., Eastwood, J. P., Cassak, P., et al. 2016, GeoRL, 43, 6060
Phan, T. D., Eastwood, J. P., Shay, M. A., et al. 2018, Natur, 557, 7704
Phan, T. D., Gosling, J. T., Davis, M. S., et al. 2006, Natur, 439, 175
Phan, T. D., Lavraud, B., Halekas, J. S., et al. 2021, A&A, 650, A13
Phan, T. D., Verniero, J. L., Larson, D., et al. 2022, GeoRL, 49, e2021GL096986
Pucci, F., Servidio, S., Sorriso-Valvo, L., et al. 2017, ApJ, 841, 60
Retinò, A., Sundkvist, D., Vaivads, A., et al. 2007, NatPh, 3, 235
Réville, V., Velli, M., Panasenco, O., et al. 2020, ApJS, 246, 24
Sanchez-Diaz, E., Rouillard, A. P., Lavraud, B., et al. 2019, ApJ, 882, 51
Sato, T., & Hayashi, T. 1979, PhFl, 22, 1189
Servidio, S., Matthaeus, W. H., Shay, M. A., et al. 2009, PhRvL, 102, 115003
Sonnerup, B. U. Ö., & Cahill, L. J., Jr 1967, JGRA, 96, 171
Stawarz, J. E., Eastwood, J. P., Phan, T. D., et al. 2019, ApJL, 877, L37
Szabo, A., Larson, D. E., Whittlesey, P., et al. 2020, ApJS, 246, 47
Viall, N. M., Spence, H. E., Angelos, V., & Howard, R. 2010, SoPh, 267, 175
Wang, R., Lu, Q., Nakamura, R., et al. 2016, NatPh, 12, 263
Wang, R., Vasko, I. Y., Phan, T. D., & Mozer, F. S. 2024, JGRA, 192, 2
Whittlesey, P. L., Larson, D. E., Kasper, J. C., et al. 2020, ApJS, 246, 74
Yin, Z., Drake, J. F., & Swisdak, M. 2024, arXiv:2401.14500v2
Zhou, M., Berchem, J., Walker, R. J., et al. 2017, PhRvL, 119, 055101